Engineering Solid Mechanics (2018) 155-174

Contents lists available at GrowingScience

Engineering Solid Mechanics

homepage: www.GrowingScience.com/esm

Investigation of intrinsic de-bonding in bonded concrete overlays: Material characterisation and numerical Study

Adegoke Omotayo Olubanwo*, John Nicolas Karadelis, Messaoud Saidani, Morteza Khorami and Samuel Jonah Abbey

School of Energy, Construction & Environment, Coventry University, Coventry, West Midlands, UK

ARTICLEINFO

Article history:
Received 26 October, 2017
Accepted 15 January 2018
Available online
15 January 2018

Keywords:
Intrinsic
De-bonding
Composite
Overlay
FEA
Restraint

ABSTRACT

This study investigates the evolution of intrinsic interfacial de-bonding of Roller Compacted Steel Fibre Reinforced Polymer Modified Concrete (RC-SFR-PMC) bonded on substrate Ordinary Portland Cement Concrete (OPCC), using both experimental and numerical techniques. The relative effects of evolving material inhomogeneity and composite dimensional stability during curing was studied as a function of overlay structural scale, using a 2D plane strain Interface Cohesive Zone Model (ICZM). The effects of creep coefficient on interface restraint capacity and ensuing cohesive zone length were clearly evaluated. The results showed that the applied curvature due to the measured shrinkage strain was inadequate to cause critical de-bonding. In the FEA results, while the rate of interface energy release generally varies as a function of the bi-material relative stiffness and overlay structural scale, it is also evident that the two variables lose effects as the overlay structural scale approaches 0.50. The overall indicative trend shows that the rate of energy release in compliant overlay when relative stiffness($\alpha<0$) is higher than when $\alpha>0$. Therefore, a more compliant overlay typically exhibits less relative restraint to bending induced de-bonding.

List of Abbreviations:

RC-SFR-PMC - Roller Compacted Steel Fibre Reinforced Polymer Modified Concrete

ICA - Interface Contact Analysis

MIV - Mathematically Independent Variable

SRM - Surface Response Methodology

AMD – Apparent Maximum Density

* Corresponding author.
E-mail addresses: aa7878@coventry.ac.uk (A. O. Olubanwo)

doi: 10.5267/j.esm.2018.1.003

TAFD - Theoretical Air Free Density

MVB – Modified Vebe

FPZ - Fracture Process Zone

OPCC – Ordinary Portland Cement Concrete

ANOVA – Analysis of Variance

1. Introduction

The basic determination of de-bonding mechanism along the interface of cementitious bi-material cast at different times requires appropriate investigation and evaluation of intrinsically induced stresses associated with inherent material asymmetry and composite dimensional incompatibility (Birkeland, 1960; Morgan, 1996; Silfwerbrand, 1997). In Bonded Concrete Overlays (BCOs), de-bonding is intrinsically induced at early-age mainly by differential shrinkage movement between the newly placed overlay and the substrate (Olubanwo et al., 2016; Olubanwo & Karadelis, 2015). Many research works have been published for investigating the mechanical properties, failure mechanisms and cracking behaviour of concretes used in construction of overlays (e.g. Rooholamini et al., 2018; Karadelis & Lin, 2017; Kim et al., 2017; Mu & Vandenbossche, 2017; Aliha et al., 2012; Guan et al., 2018; Enfedaque et al., 2017; Fakhri et al., 2017; Kim & Bordelon 2017; Heidari-Rarani et al., 2017). From continuum perspective, it has been shown that the interface experiences intrinsic self-equilibrating stresses as a result of consequential eigen-strain inhomogeneity of the system (Myasnikov et al., 2004). Thus, under cumulative stresses and subsequent interfacial bond degradation, less and less stresses are transferred across the plane of the interface until de-bonding or true cracks develop (Nawy & Ukadike, 1983; Suprenant, 1988). Such progressive interfacial failure is well understood within the domain of linear elastic or nonlinear fracture mechanical analysis, depending on the initial geometric condition of the bonded plane (Chandra, 2002; Carlsson & Prasad, 1993; Cornec, et al., 2003). Though, several analytical techniques exist on how to estimate the resulting mixed-mode de-bonding parameters; the underpinning generic approach relies on expanding the conjugate variables of the de-bonding failure parameters in the normal and tangential planes (Turon et al., 2007; Olubanwo et al., 2017). From here, both effective traction vector and its corresponding displacement are formulated for de-bonding initiation and propagation. This paper investigates via laboratory based experiments and finite element analysis technique the significant evolution of interfacial de-bonding failure associated with intrinsic loadings and material asymmetry between two bonded concrete materials. Distinct 2D plane strain numerical cases involving variable structural scale, creep coefficient and crack-tip phase-angle effects were considered within the context of zero-thickness Interface Contact Analysis (ICA).

2. Theoretical Basis

It is well-known that the exact solution of the continuum interactions or interfacial decohesion of concrete laminates under extrinsic or intrinsic loading is non-trivial. This is because the extreme assumptions associated with various limit analysis and classical energy-based failure approaches such as Linear Elastic Fracture Mechanics make them unsuitable for quasi-brittle material like concrete (Caballero et al., 2008; Charalambides et al., 1990). As such, successful description of the interface behaviour requires a robust approach where both de-bonding initiation and propagation are unified within a single model. This is possible, and can be implemented numerically using Interface Contact Analysis associated with a prescribed Cohesive Material Law.

2.1. Interface Contact Analysis

The application of Interface Contact Analysis is concerned with two essentials, namely: (1) determination of contact stresses transmitted across the interface, and (2) ensuring that interfacial

compatibility (impenetrability) condition is enforced during de-bonding analysis. Thus, the overall evaluation of the mechanical responses in this paper was based on the imposition of geometric constraints and the application of the governing constitutive law. Constraint formulations were applied for both normal and tangential contact conditions under a mixed mode de-bonding condition. The non-penetration conditions for normal contact, for instance, was mathematically enforced when the bond gap $(u_N) \geq 0$. The conditions for decohesion then correspond to $P_N = 0,\ u_N > 0$, so that the actual cohesion/adhesion condition is given by $P_N < 0,\ u_N = 0$. The resulting tractions (P) in the normal and tangential directions are generally given by:

$$P = \begin{cases} P_N = k_N u_N & for\ \ Normal \\ \tau = k_T u_T & for\ \ Tangential \end{cases} \tag{1}$$

where, P_N and τ are the contact stresses in the normal and tangential directions respectively, k_N and k_T are the corresponding contact stiffnesses, and u_N and u_T are normal and tangential separation or slip. By considering an Augmented Lagrange Penalty based stiffness formulation the above normal contact force corresponds to:

$$P_N = \begin{cases} 0, & if\ u_N > 0 \\ k_N u_N + \lambda_{i+1} & if\ u_N \leq 0 \end{cases} \tag{2}$$

where,

$$\lambda_{i+1} = \begin{cases} \lambda_i + k_N u_N, & if\ |u_N| > \epsilon \\ \lambda_i & if\ |u_N| < \epsilon \end{cases} \tag{3}$$

$$\epsilon = compatibility\ or\ penetration\ tolerance$$

The above augmented method involves the update of the penalty stiffness during numerical iterative series via a multiplier (λ). The approach is generally less sensitive to the value of the contact stiffness (k_N) specified because the value of the multiplier (λ) is increased accordingly as an adjustment such that the maximum allowable penetration tolerance (ϵ) is not exceeded during the solution process. This is particularly desirable because stiffness intrinsically changes with both material and geometric responses during loading. Note, as in normal contact case, a Lagrange multiplier (λ_T) was also associated with the frictional contact formulation accordingly, so that the total potential energy $(\delta\Pi)$ assumes:

$$\delta\Pi = \int_\Gamma [(\lambda_N + k_N u_N)\delta u_N + (\lambda_T + k_T u_T)\delta u_T]\, dA, \tag{4}$$

where, λ_N and λ_T are Lagrange multipliers associated with de-bonding in the normal and tangential directions.

Here, the frictional constitutive equation adopted was the classical Coulomb's interface law based on two distinguishable regimes, namely - sticking and slipping. Thus, by first assuming an elastic slip process based on associative tangential contact stiffness, the usual non-smooth interface load vs slip contact behaviour is circumvented. As such, the resulting frictional stress is given by:

$$\tau = \begin{cases} \tau_i^{n-1} + k_T \delta u_{Ti}, & if\ \ /\tau/ = \sqrt{{\tau_1}^2 + {\tau_2}^2} - \mu_{iso} P_N < 0\ (for\ sticking) \\ \mu_{iso} P_N \dfrac{\delta u_{Ti}}{/\delta u_T/}, & if\ \ /\tau/ = \sqrt{{\tau_1}^2 + {\tau_2}^2} - \mu_{iso} P_N = 0\ (for\ sliding) \end{cases} \tag{5}$$

The condition for sliding corresponds to:

$$/\tau/ \geq \tau_{lim} \tag{6}$$

where, $\tau_{lim} = limit\ shear\ stress$, defined by:

$$\tau_{lim} = c + \mu_{iso} P_N \tag{7}$$

$$/\tau/ = \begin{cases} |\tau| & (equivalent\ shear\ stress\ for\ 2D\ contact) \\ \sqrt{{\tau_1}^2 + {\tau_2}^2} & (equivalent\ shear\ stress\ for\ 3D\ contact) \end{cases}$$

$\mu_{iso} = isotropic\ coefficient\ of\ friction$;
$\delta u_{Ti} = slip\ increament\ in\ direction\ i\ over\ the\ current\ substep$
$/\delta u_T/ = equivalent\ slip\ increament\ over\ the\ current\ substep$
$\tau_i^{n-1} = frictional\ stress\ in\ direction\ i\ at\ the\ end\ of\ previous\ substep$
$c = contact\ cohesion$

As it is, the frictional interface response in sticking condition is reversible, hence the relative tangential velocity is zero during loading; otherwise, relative slip is mobilized, and the tangential velocity takes a non-zero value (Olubanwo & Karadelis, 2015). Therefore, a rational treatment of the frictional contact with elasto-plastic concepts will require additive decomposition of the interface into its undamaged elastic regime and plastic damaged part in accordance to Eq. (8):

$$\begin{cases} \dot{u}_T = 0 \Leftrightarrow \delta_T = 0 & (for\ sticking) \\ u_T = u_T^e + u_T^p & (for\ slipping) \end{cases} \tag{8}$$

where, $\dot{u}_T = relative\ tangential\ velocity$; $u_T = tangential\ elastic\ (micro) slip$
$u_T = total\ tangential\ slip$; $u_T^e = elastic\ tangential\ micro\ displacement$
$u_T^p = plastic\ tangential\ displacement$

Note that with the above decomposition, a regularization step for frictional law is implied. To achieve a smooth friction law, a regularization of Coulomb's law was assumed based on the non-associative slip rules of the theory of plasticity. The well-known associative flow-rule is common with metals; but for frictional materials like concrete and rocks, non-associative formulations are used in the sense that they exhibit significant pressure sensitivity (Caballero, et al., 2008). Frictional interface of this type also exhibits dilatancy due to concurrent interface de-cohesion and sliding in both normal and tangential directions respectively, but dilatancy invariably loses effect with increased compression or interface sliding progression. As it were, the variational dependencies of interfacial bond strength and dilatancy on normal stress therefore leads to non-associative formulations.

2.2 Interface Cohesive Material Law

In addition, the complex tractions across the interface of the bi-material was evaluated and described numerically using ANSYS Interface Contact Analysis associated with a Bilinear Cohesive Material Law. The Cohesive law is based on reversible or irreversible traction-displacement law described in (Alfano and Crisfield, 2001; Bower, 2010). The latter typically leads to the creation of new stress free adjacent surfaces. This damage approach is contingent on specifying a damage parameter needed to quantify the cumulative irreversible damage induced on the interface. For instance, in the bi-linear softening relation shown in Fig. 1(a), the damage parameter (d_n) evolves from 0 to 1, hence the de-bonding parameter is given by:

$$d = \begin{cases} 0 & for\ \ u_N = \bar{u}_N \\ 0 \leq d_n \leq 1 & for\ u_N > \bar{u}_N \end{cases} \tag{9}$$

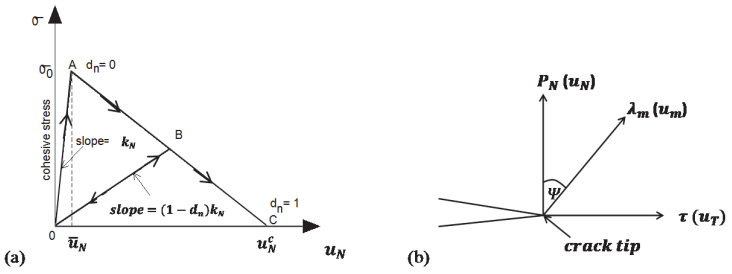

Fig. 1. (a) Bilinear softening relation and (b) Mixed-mode stress and displacement fields

The reversible regime is depicted by line OA when the interface initially deforms elastically with a constant stiffness (k_N). Subsequently along line ABC, the interfacial stress decreases linearly with the displacement ($\overline{u}_N \leq u_N \leq u_N^c$). During accumulated irreversible damage, the interfacial stiffness drops such that in its unloading state the traction-displacement now follows a reduced linear slope BO. $\overline{u}_N$ and u_N^c are the critical separation for de-bonding initiation and propagation respectively, u_N represents the accompany interfacial separation, while its tangential counterpart is denoted by u_T (see Fig. 1(b)). For the mixed-mode conditions, the conjugate variables of the de-bonding are expanded in both normal and tangential directions such that the criteria for damage initiation and propagation now accounts for the concomitant effects of Mode I and Mode II fractures. Thus, from Fig. 1(b), the de-bonding driving energy is numerically assumed to be controlled by the local steady-state phase angle ($\Psi = tan^{-1}\left(\frac{\tau}{\langle\sigma\rangle}\right)$) associated with the oscillatory field within the vicinity of the crack tip. The interface therefore attains its critical fracture condition when the mixed-mode energy release rate G_{ic} equals the fracture toughness of the interface $G_{ic}(\Psi)$. From here, the magnitude of the normalised mixed-mode de-bonding driving energy defined by equation (10) is estimated as a three-parameter function, namely: overlay structural scale $\eta = \left(\frac{h_{overlay}}{h_{total}}\right)$, bi-material relative stiffness $\alpha = \left(\frac{E_1' - E_2'}{E_1' + E_2'}\right)$ and relative compressibility $\beta = \left(\frac{E_1'(1-v_1)(1-2v_2) - E_2'(1-v_2)(1-2v_1)}{2(1-v_1)(1-v_2)(E_1' + E_2')}\right)$.

$$G_{ic} = D_c(\eta, \alpha, \beta) = \frac{E^* G_{ic}(\Psi)}{\lambda_m^2 h_{overlay}} \tag{10}$$

where, $E^* = \frac{1}{2}\left(\frac{E_1' . E_2'}{E_1' + E_2'}\right)$; $\lambda_m = \sqrt{\langle P_N\rangle^2 + \tau^2} = \frac{\langle P_N\rangle}{Cos\,\Psi} = \frac{\tau}{Sin\,\Psi}$; $h_{overlay}$ is overlay thickness; α and β are Dundur's mismatched elastic properties (Dundurs, 1969); $E_i' = E_i/(1 - v_i^2)$.
Note, equation (10) typically corresponds to an extended Hillerborg's characteristic length (Hillerborg et al., 1976; Petersson, 1981) which permits the de-bonding driving coefficient (D_c) to be numerically evaluated as a function of the structural scale (η) for different values of α when a non-zero value of β is fixed. Here the effect of non-zero value of β is small and typically assumed insignificant (Buyukozturk and Hearing, 1998). In this investigation, the effects of stress relaxation due to the viscoelastic property of the overlay material was incorporated into equation (10) via the estimated values of the creep coefficient [$\phi(t, t_0)$] given in the next sections (i.e. Fig. 10c).

3. Methodology

The research approach and procedures followed in this investigation is shown in Fig. 2. The method adopts a unified experimental and numerical technique. The unified technique involved the following sequential steps:
(1) Selection of mixture modelling technique, and identifying multi-criteria optimum wet responses via initial desirability goal setting; (2) Mixture model idealization and material phase classification; (3) Initial mixture components screening and subsequent reduction of (q) mixture components to ($q - 1$) independent mixture-related variables using mathematically independent variable (MIV) experiment

design approach; (4) Mixture model formulation based on a $2^{(q-1)}$ factorial design, augmented with $2 \times (q-1)$ axial points and at least 3 centre points; (5) Mixture testing and characterization (fresh state); (6) Individual and composite desirability weighing and checking; (7) Result verification; (8) Overlay material and interface bonding testing and characterisation; (9) Intrinsic strain measurement and estimation; (10) Numerical modelling, analysis and simulations.

3.1. Material Modelling and Characterisation

This section considers overlay material selection, mix formulation and its applicability quality assessment using mathematically independent variable (MIV) experiment design approach described in (Box & Draper, 1987). Surface Response Methodology (SRM) was implemented for the mix design space during which (q) mixture components were reduced to $(q-1)$ independent mixture-related variables. The applicability quality of the roller compacted overlay material in its plastic state was measured in terms of the consistency MVB (Modified-Vebe test) performance and Apparent Maximum Density (AMD). As a generic guide, effective consolidation is assumed when the mix is dry enough to prevent sinking of the vibrating equipment, but sufficiently wet to allow paste content distribution during placing.

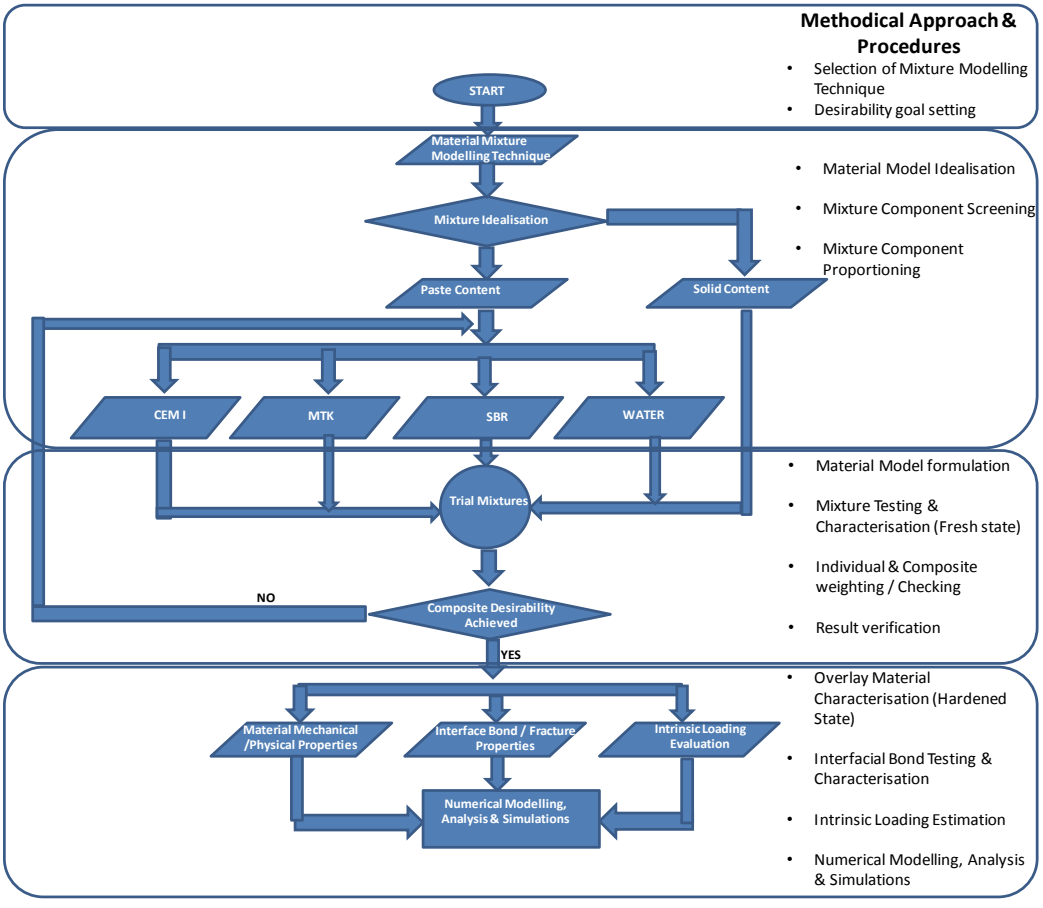

Fig. 2. Research Approach and Procedures.

3.2. Overlay Mix Formulation

The overlay Roller Compacted Steel Fibre Reinforced Polymer Modified Concrete (RC-SFR-PMC) was designed to achieve optimum consolidation at relatively low water-binder ratio in its plastic state.

Mix Consistency and Apparent Maximum Density (AMD) requirements complied with the test procedures described in ASTM C1170 / C1170M (2008) and ASTM D792 (2008) respectively. The best consolidated mix which supports vibration effectively is expected to yield overlay with best density, strength and interface bonding. Enhanced composite compatibility requirement in terms of movement-related properties was consequently achieved by ensuring adequate substrate aggregate interlocking action, and by avoiding aggregates with high thermal coefficient and water absorption. The combined aggregate grading graph is illustrated in Fig. 3.

The formulation of the experimental mixture space was based on varying the constituent components of the mixture within their predefined practical upper (U_i) and lower (L_i) bounds. The SRM mixture model was subsequently implemented on the assumption that the mixture capacity to support roller vibration is dictated largely by the paste-phase; thus only components constituting the paste-phase were varied accordingly. The amounts of constituents forming the solid-phase of the mix were thus held constant sequel to a previous work in (Olubanwo and Karadelis, 2015). The overall treatment of the experimental mixture space was based on a $2^{(q-1)}$ factorial design, augmented with $2 * (q - 1)$ axial points and 3 centre points. In the analysis, the three independent variables used to describe the system are given by: $x1 = WATER$; $x2 = SBR$; and $x3 = \frac{MTK}{(CEM\ I + MTK)}$. The mixture experiments therefore investigate variable combinations of the paste constituents that will be required for optimal desirability performance when mixed with a constant proportion of the solid constituents given in Table 4. In addition, the composite desirability was achieved using the optimisation function (D) defined by $D = [d(y_1) * d(y_2) * \ldots\ldots\ldots * d(y_n)]^{1/n}$. Note, n represents the number of all individual responses involved in the analysis, while ($d(y_i)$) is the individual desirability function. Here, the desirability scale for each response measured for each possible mix is constrained within $0 \leq d(y_i) \leq 1$. The conditions for acceptance or rejection therefore depend on whether the optimisation goal is aiming for a target, maximised or minimised.

3.3. Mixture Variability Range, Testing & Analysis

In ACI guidelines (ACI 548.1R-92; ACI 548.4-93), high cement content in the range of 600 – 700 kg/m^3 is recommended for bridge deck and pavement overlays materials modified with Styrene-Butadiene Rubber (SBR) to ensure sufficient interfacial bonding and overlay strength development. But in order to minimise the risks of high drying shrinkage and thermal cracking in the overlay material (without necessarily compromising bonding and strength development), partial cement replacement was incorporated with Metakaolin (MTK). Cementitious contents ($CEM\ I + MTK$) were varied between 581.9 kg and 623 kg in 1m^3 of the total mixture. These correspond to about 0.394 and 0.285 of $\frac{MTK}{(CEM\ I + MTK)}$ respectively. Also, the trial range of variabilities for $\frac{WATER}{(CEM\ I + MTK)}$ and $\frac{SBR}{(CEM\ I + MTK)}$ were constrained between 18% & 22% and 10% & 15%, respectively. Thus, by setting the upper and lower range for the mixture variables, 17 possible mix combinations were experimentally implemented and analysed, comprising 8 factorial points, 6 axial points and 3 centre points per run. A total of three runs were carried out for each factorial and axial point. The Analysis of Variance (ANOVA) and Composite Desirability analysis were subsequently performed with Minitab statistical software (Version, 17) based on a two-response desirability goal shown in Table 3. In the ANOVA, components and models with p-value ≤ 0.05 were selected as viable.

The mixing procedure for each batch followed (ASTM C1439-99 (1999), while the resulting Apparent Maximum Density (AMD), Air-Content (%) and Theoretical Air Free Density (TAFD) were determined using the procedures given in ASTM C138 (2001) and ACI 211.3R (2002). As shown in Fig. 5, the optimum mixture achieved full consolidation at 35 seconds with a corresponding AMD of 98.69% TAFD. The observed value of AMD shown here falls above the minimum AMD of 96%TAFD required for most Roller Compacted Concrete pavement overlay materials. Fig. 4(a,b) shows the contour plots for the measured Consistency-time and the corresponding AMD as a percentage of TAFD.

Fig. 5(c) shows the optimal composite desirability response curves based on the input variable settings given in Table 3. As seen, the optimal composite desirability "D" and the individual desirability depicted by "d" for each predicted property show sufficient closeness to 1. From the results, the predicted optimum response "y" associated with each measured property is also given. The optimum mixture proportion is indicated by the square brackets at the top of each column in Fig. 5(c) where: WATER=118.5 6kg, SBR=76.81 kg, and $\frac{MTK}{(CEM\ I+MTK)}$= 0.283. From here, the required quantities of MTK and CEM I were estimated based on the limiting quantity of the paste content in the total mix estimated to be 797.4 kg. Table 1 and Table 2 show the constituents' specification, composition and properties, while Table 4 gives the resulting optimum constituents for the overlay and the substrate OPCC by weight.

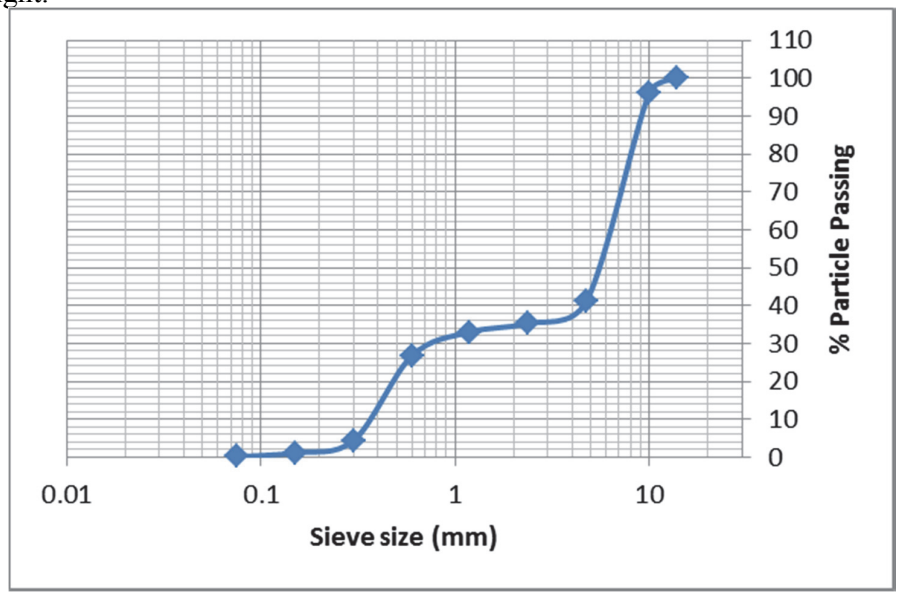

Fig. 3. Combined Aggregate grading graph

Table 1. Composition and Properties of CEM I (HANSON HEIDELBERG, UK)

Physical Properties	**Chemical Composition by weight (%)**								
Loss on ignition	Cl	SiO_2	Fe_2O_3	Al_2O_3	MgO	CaO	K_2O	SO_3	Na_2O
3.3%	0.05	20.06	2.67	4.42	1.19	64.04	0.71	3.1	0.21

Note: CEM I, 52.5N

Table 2. Composition and Properties of Metakaolin (AGS MINERAUX, FRANCE)

Physical Properties			**Chemical Composition by weight (%)**					
			SiO_2	TiO_2	Fe_2O_3	Al_2O_3	CaO+MgO	Na_2O+K_2O
Loss on ignition	Pozzolanic index	Specific area						
1%	1100 mg $Ca(OH)_2$/g	17 m2/g	55	1.5	1.4	40	0.3	0.8

Note: MTK=White powder, loss on ignition 1%, water demand (Mars cone) 900 g/kg

Table 3. Summary of two-response desirability goal

Measured Property	***Goal***	***Lower***	***Target***	***Upper***	***Weight***
Consistency-time (sec)	Target	24.4	35.0	39.3	1
Compacted density (%TAFD)	Maximize	96	98.0	-	1

Table 4. Optimum RC-SFR-PMC & OPCC Material Constituents

Measured Quantity	Binder Phase Constituents				Solid Phase Constituents			Total
	CEM I	MTK	SBR	Water	CA	FA	SF	
RC-SFR-PMC Quantity (kg) in 1m^3	432.14	169.89	76.81	118.56	930.72	640.8	117	2485.92
Specific/particle density (Kg/m^3)	3,150	2,507	1,040	1,000	2,770	2,670	7,800	-
Volume in 1m^3	0.137	0.068	0.074	0.119	0.336	0.240	0.015	0.988
OPCC Quantity (kg/m^3)	400.00	-	-	200.00	1116.00	684.00	-	2400

Note: SBR (Styrene-Butadiene Rubber)=White emulsion, solid content 46%, water content 54%; Steel Fibre (SF) Length 35mm, hooked-end, aspect ratio 60, tensile strength 1050MPa; CA (Coarse aggregate)= Crushed gritstone; size 4.75 -10mm, water absorption 0.5%, particle density on saturated surface-dried 2770 kg/m^3; FA (Fine Aggregate)= Quartz river sand, water absorption 0.5%, fineness modulus 2.48, particle density 2670 kg/m^3; OPCC=Ordinary Portland Cement Concrete; RC-SFR-PMC Air Content (%)=100$\left(\frac{T-D}{T}\right)$ = 1.2%; T=TAFD=$\left(\frac{Mass\ of\ contituents\ (kg)}{Total\ Absolute\ Volume\ of\ constituents\ (m^3)}\right)$ = 2516.11kg/m^3; D=density or unit weight =2485.92kg/m^3.

Table 5. Regression models for Consistency-time, AMD, and Compacted density

Property	Model Equations	R-sq.
Consistency-time(sec)	-244.7 + 3.4 (x_1) + 2.9 (x_2) + 21.8 (x_3) - 0.009 $(x_1)^2$ − 0.007 $(x_2)^2$ + 47.4 $(x_3)^2$ - 0.02 x_1x_2 - 0.79 x_1x_3 + 0.61 x_2x_3	98.7
AMD (%TAFD)	-156.9 + 3.4 (x_1) + 1.6 (x_2) - 28.6 (x_3) - 0.013 $(x_1)^2$- 0.006 $(x_2)^2$ − 13.6 $(x_3)^2$ - 0.006 x_1x_2 + 0.41 x_1x_3 - 0.15 x_2x_3	97.4
Compacted density(kg/m^3)	-3901 + 84.55 (x_1) + 38.77 (x_2) - 71 (x_3) - 0.32 $(x_1)^2$ - 0.14 $(x_2)^2$ − 339 $(x_3)^2$ - 0.14 x_1x_2 + 10.06 x_1x_3 - 3.73 x_2x_3	97.4

where: R-sq = *Coefficient of determination; :* $x1 = WATER$; $x2 = SBR$; and $x3$= $\frac{MTK}{(CEM\ I+MTK)}$

As shown in Fig. 5, the curve under each material constituent shows the wet property responses as each paste component used in the computational experiment varies between its upper and lower limits. The constraints are done such that when one component increases, other components decrease accordingly. As depicted in Fig. 5 (c) quantities of constituents below or above the optimum, lower the overall desirability mixture performance/quality in terms of practical applicability. The regression model equations based on the constituents' interaction are given in Table 5 with their respective coefficients of determination (R-sq). In the three-run validation tests based on the optimum mix given in Table 4, the ring of mortar (see Fig. 5 (a,b)) actually formed at 36 seconds, while the electric plate vibrated AMD yielded 2468.30 kg/m^3, about 98.1% of the mix's TAFD. These values are sufficiently within the predicted results in Fig. 5(c).

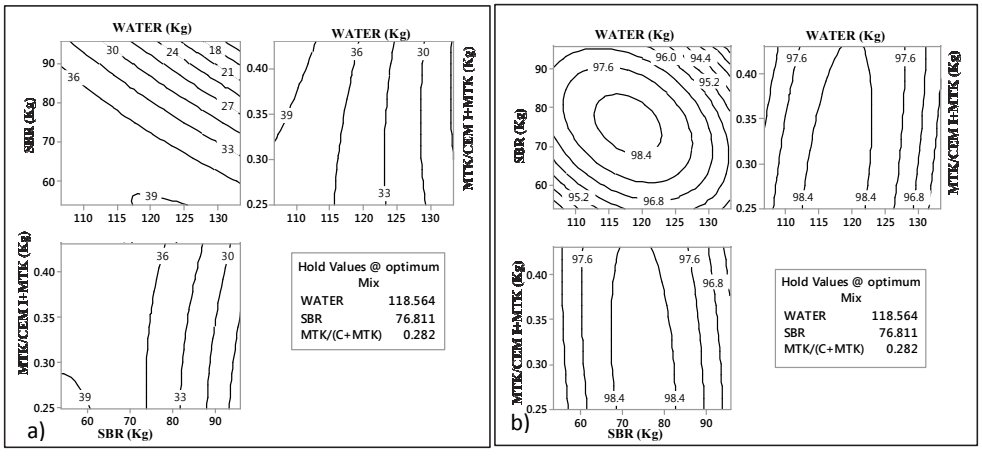

Fig. 4. (a) Contour Plots of (a) Consistency time (sec) (b) AMD (%TAFD)

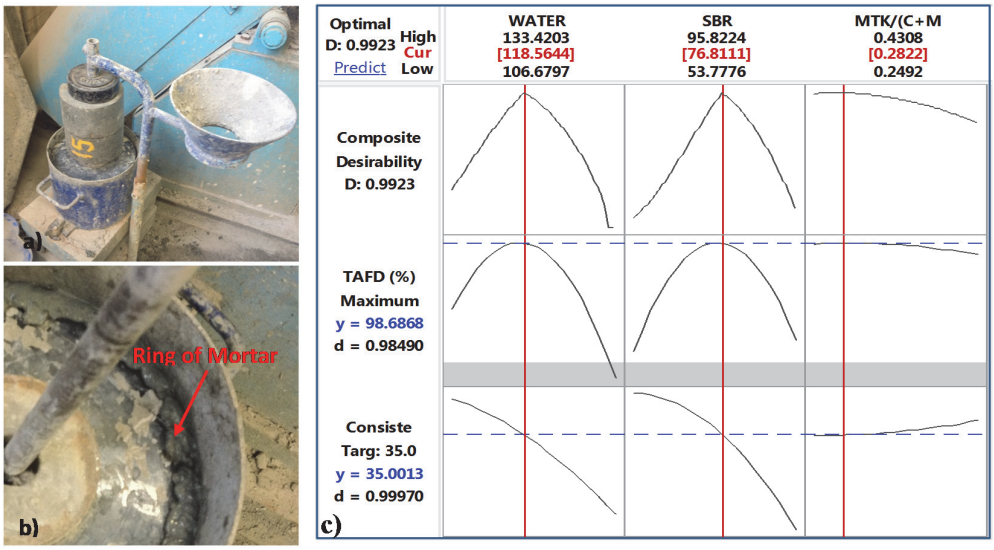

Fig. 5. (a) 22.7 kg surcharge mass mounted on test specimen, (b) Fully consolidate test specimen with a ring of mortar around the disk (c) Composite optimization Response plot

3.4. RC-SFR-PMC Mechanical & Fracture Properties determination

Compressive and elastic modulus was determined from cylindrical specimens made of 200 mm high by 100mm diameter. Tests were performed at 3, 7, 14, 28, 56 and 90 days in accordance to ASTM C469/C469M (1994) procedures. Each cylinder used for elastic modulus determination was instrumented with 60 mm strain gauges (120±0.3Ω) in the longitudinal and lateral directions as shown in Fig. 6. Additional parameters measured included the splitting tensile strength in accordance to BS EN 12390-6 (2000). Four specimens were tested for each experiment. Prior to testing, specimens were cured in the moulds and covered with polythene sheets at 65% RH laboratory condition for 24 hours. Afterward, specimens were de-moulded and stored in the curing tank at 100% RH for 48 hours followed by laboratory air curing until testing. The corresponding measured values are shown in Fig. 7. At early age 3, the measured mean Compressive and Splitting tensile strengths were 31.39 MPa and 3.34 MPa, respectively, while the Elastic modulus yielded 16.68 GPa for the same age.

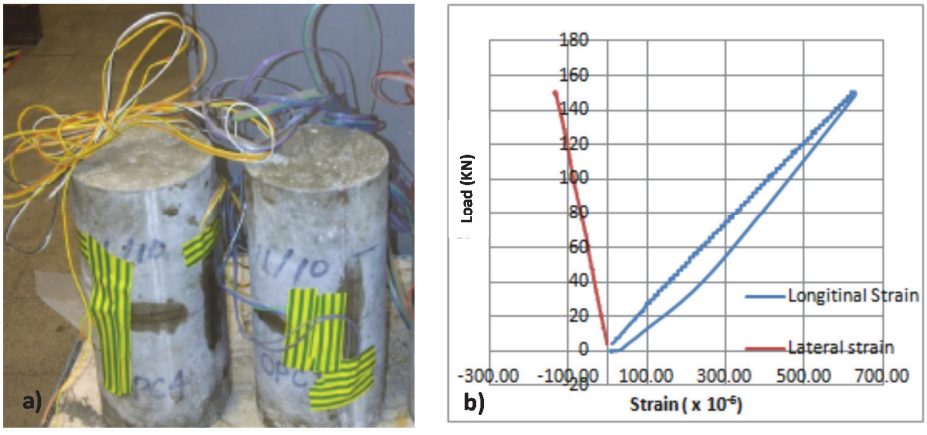

Fig. 6. (a) Strain Gauged Specimens for Elastic modulus & Poisson's ratio measurement (b) Typical Load vs Stains under compressive loading

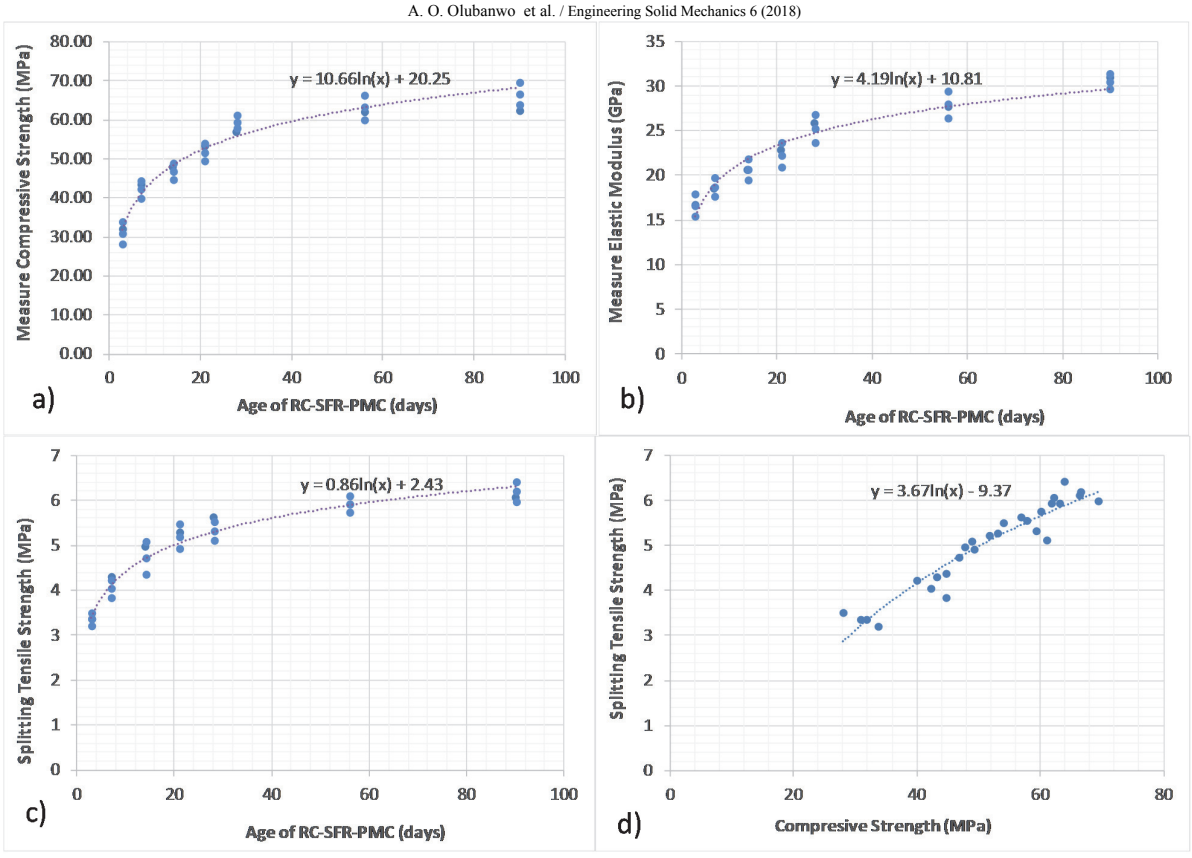

Fig. 7. (a) Mean compressive strength (b) Mean Elastic Modulus (c) Mean Splitting tensile strength (d) Graph of Mean splitting tensile strength vs Mean compressive strength

For composite fracture testing, stress transmission across the interface of RC-SFR-PMC and OPCC were assessed in terms of shearing, tensile resistant and toughness capacity. The substrate OPCC surface was roughened with rubber brushing to an average depth of 2.4 mm five hours after casting into the moulds. Similar procedure has been implemented elsewhere (Olubanwo & Karadelis, 2015). Sand-patch method in accordance to BS 598-3 (1985) was used to measure the degree of roughness prior to placing and compacting of RC-SFR-PMC on the prepared substrate OPCC. Composite splitting tensile (Brazilian test) were performed in accordance to ASTM C496/C496M-11 (2011), while the direct shearing test adhered to IDOT (2000). Four replicas were tested for each bond test. Detailed set-up for both experiments are shown in Fig. 8.

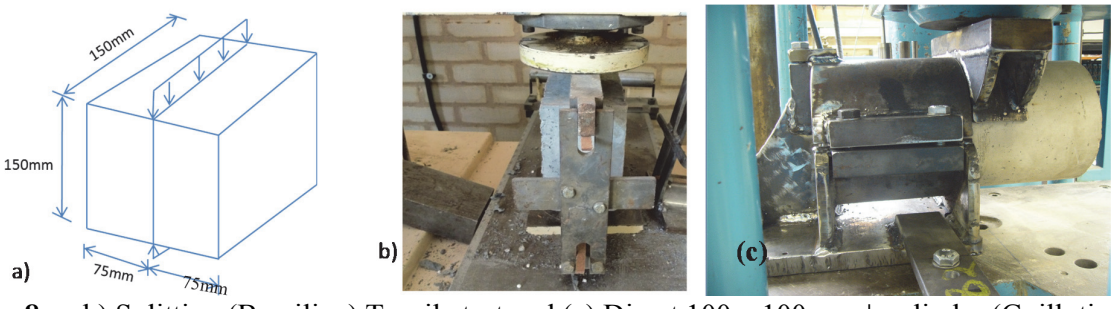

Fig. 8. a, b) Splitting (Brazilian) Tensile test and (c) Direct 100 x 100mm ϕ cylinder (Guillotine) Shear test

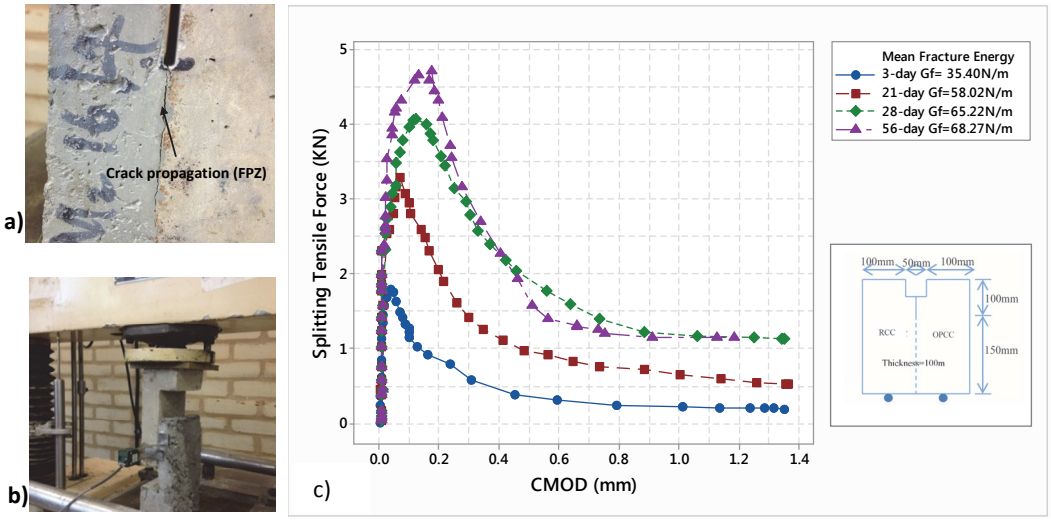

Fig. 9. (a) Wedge Splitting set-up & Crack propagation and (b) Direct L-Prism shear test with clip gauge (c) Wedge Splitting Force vs. Crack Mouth Opening Displacement

The ultimate bond capacity tests shown in Fig. 8 only illustrate the interfacial de-bonding initiation stage at peak stress, additional fracture process zone (FPZ) tests such as Wedge-splitting tensile and L-Prism shear experiments shown in Fig. 9 (or other specimens like semi-circular bend SCB specimen given in Mirsayar et al. (2017) are required to fully characterise and describe the progressive or phenomenological failure of the interface. In both experiments, test specimens were controlled monotonically at 0.0012 mm/s by increasing the displacement until the samples failed. The magnitude of the horizontal splitting force relative to CMOD was estimated using :$\left(P_H = \frac{P_V}{2tan\theta}\right)$; where P_V= vertical compressive force, and θ= wedge angle in degree. In order to estimate the interface fracture energy, the P_H vs. CMOD was plotted, and the area under the graph was calculated, which represents the work of fracture. The ultimate fracture energy was determined by dividing the work of fracture by the area of the bonded ligament. Representative response graphs per age are illustrated in Fig. 9 (c), while Table 6 shows the range of measured interfacial properties from L-Prism shearing, Wedge-splitting and Brazilian tensile splitting tests.

Table 6. Range of Measured Fractured Properties

Age (days)	Tensile Bond strength (σ_0) (N/mm^2)	Shear Bond Strength (τ_0) (N/mm^2)	Fracture toughness (G_{fII}) (N/m)	Mean Critical shear slip (u_t^c) (mm)	Mean Critical opening (u_n^c) (mm)
3	2.10	3.31 ± 0.19	143 ± 5.42	0.111	0.030
21	2.37	3.87 ± 0.21	215 ± 6.16	0.120	0.049
28	2.50	4.17 ± 0.05	271 ± 4.05	0.129	0.052
56	2.61	4.28 ± 0.08	277 ± 2.84	0.127	0.052

3.5. Shrinkage Strain Measurement & Creep parameters Estimation

The RC-SFR-PMC overlay free drying shrinkage measurement was implemented using prism specimen size (80 x 80 x 230 mm) shown in Fig. 10(a). In order to maintain a constant temperature, the test specimens were stored with all sides equally exposed in the temperature controlled room at 25^0C and 60% humidity. In addition, drying shrinkage on restrained RC-SFR-PMC overlay was measured using the composite beam shown in Figure 10(b). Restrained shrinkage strains were measured at three designated Demec points shown on the beam. The substrate was made of OPCC beam prism cast and cured in laboratory air curing condition for 90 days prior to placing the RC-SFR-

PMC overlay. Surface preparation was implemented by rubber brushing five hours after casting the OPCC into the moulds. In Fig. 11, the measured shrinkage stain results are illustrated with the estimated creep parameters based on the procedures given in EC2 ANNEX B (BS EN, 1992).

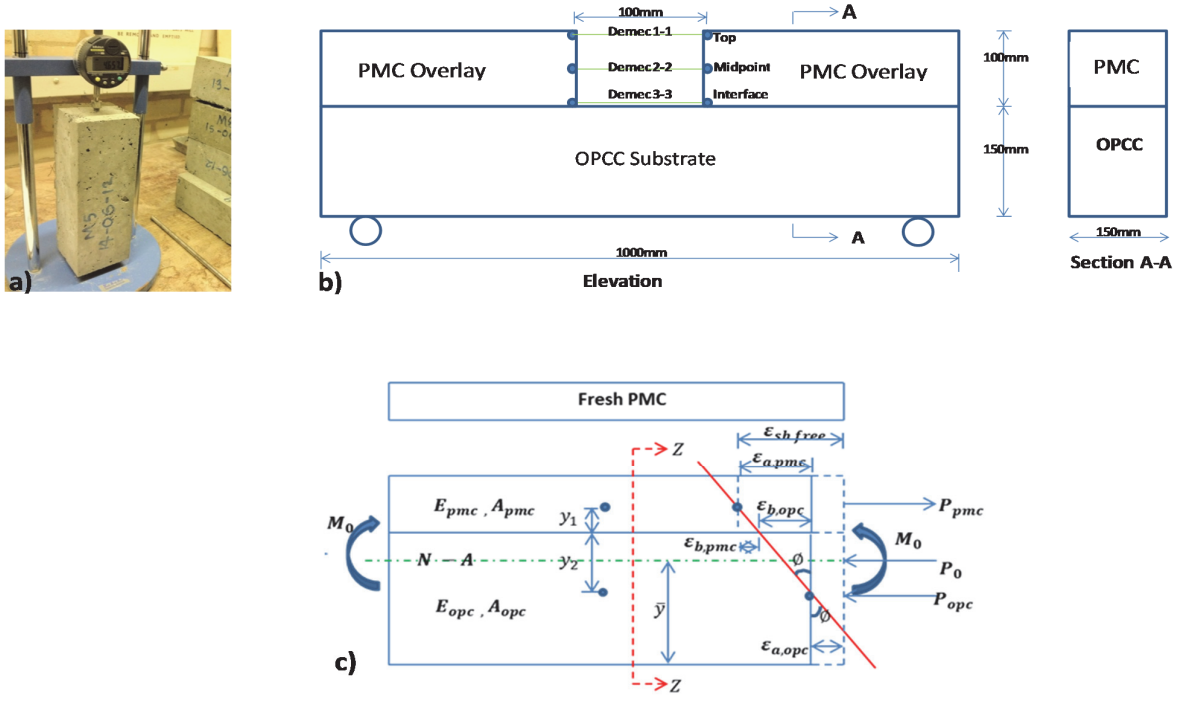

Fig. 10. Drying shrinkage set-up (a) Free condition (b) Restrained condition (Roughness=2.4mm – sand patch method) (c) Bi-material Composite section under Intrinsic Actions

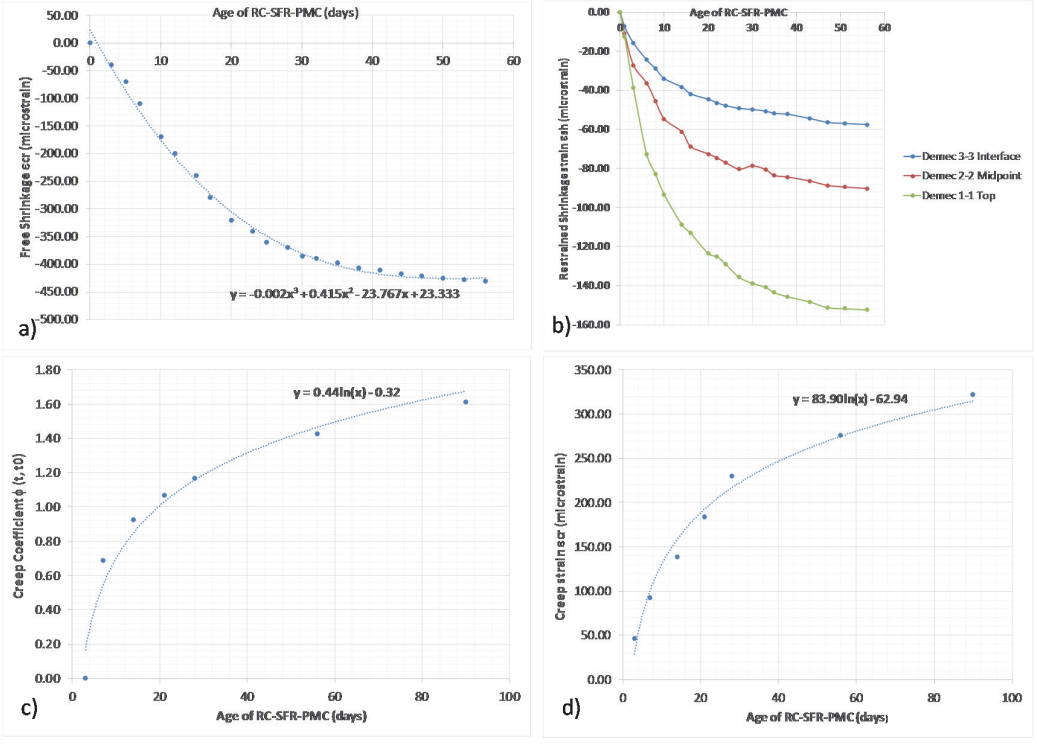

Fig. 11. Drying shrinkage measurements (a) Free Shrinkage Strain (b) Restrained Shrinkage Strain (c) Estimated Creep Coefficient (d) Estimated Creep Strain

As seen in Fig. 11(a), the measured overall free drying shrinkage at 56 days is less than 450 microstrains. This value is however by far larger than the restrained shrinkage strains shown in Figure 11(b). The measured restrained strain within the vicinity of the interface is found to be about 2.6 times lesser than the measured strain at the top of the overlay. The region of the interface therefore experiences more intrinsic stresses than any other region of the overlay which at critical bond capacity will cause the overlay to peel off. Note here that the total peeling strain on the composite test specimen will correspond to the sum of the measured shrinkage strain and the estimated creep strain shown in Fig. 11(d). However, due to its viscoelastic property, stresses in the overlay may be relieved by the creep coefficient whose estimated values are shown in Fig. 11(c). With reference to Fig. 10c, assuming a no-slip interface condition, the magnitude of the intrinsic strain actions on the composite section is given by:

$$\varepsilon_{sh.free} = \varepsilon_{b,pmc} + \varepsilon_{b,opc} + \varepsilon_{a,opc} \tag{11}$$

The bending strain generally corresponds to:

$$\varepsilon = y\emptyset = \frac{y}{\rho} \tag{12}$$

$$\text{Thus, } \varepsilon_{sh.free} = y_1\emptyset + y_2\emptyset + \varepsilon_{a,opc} \tag{13}$$

So that the curvature $\emptyset$ yields: $\emptyset = \frac{\varepsilon_{sh.free} - \varepsilon_{a,opc}}{y_T}$, where, $y_T = y_1 + y_2$ as shown in Fig. 10(c). Further, considering equilibrium of forces between P_{pmc} and P_{opc}, $\varepsilon_{a,opc} = \frac{\varepsilon_{a,pmc}(EA)_{pmc}}{(EA)_{opc}}$. Hence, the final curvature equation becomes:

$$\emptyset = \frac{\varepsilon_{sh.free} - \left(\frac{\varepsilon_{a,pmc}(EA)_{pmc}}{(EA)_{opc}}\right)}{y_T} \tag{14}$$

where, $\varepsilon_{sh.free}$= measure free shrinkage; $\varepsilon_{b,pmc}$= bending strain in PMC overlay; $\varepsilon_{b,opc}$= bending strain in OPCC; $\varepsilon_{a,opc}$= axial strain in OPCC if not fully axially restrained; $(EA)_i$= axial stiffness of an ith material in the composite; $\varepsilon_{a,pmc} = \frac{\sigma_{a,pmc}}{E_{pmc}}$ = net axial strain in the overlay pmc.

The resulting net peeling strain (analytical) estimated from Eq. (12) and Eq. (14) due to values extrapolated from Fig. 11(a,d) is shown in Fig. 12. This value falls within close proximity of the experimental and the equivalent no-slip 2D plane strain FEA results shown in Fig. 12 and Fig. 13.

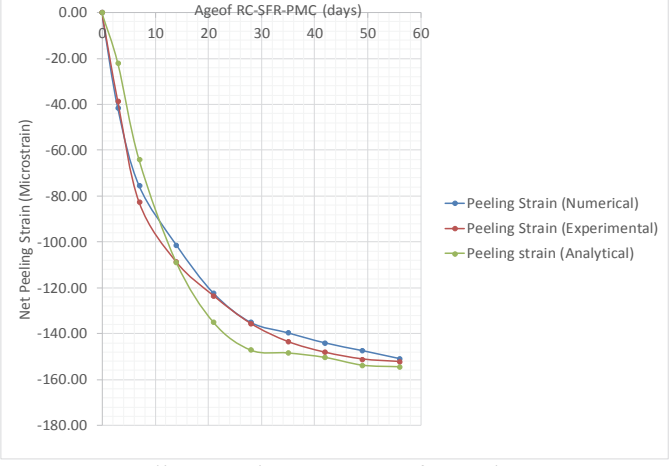

Fig. 12. Net Peeling Strains vs. Age of Overlay RC-SFR-PMC

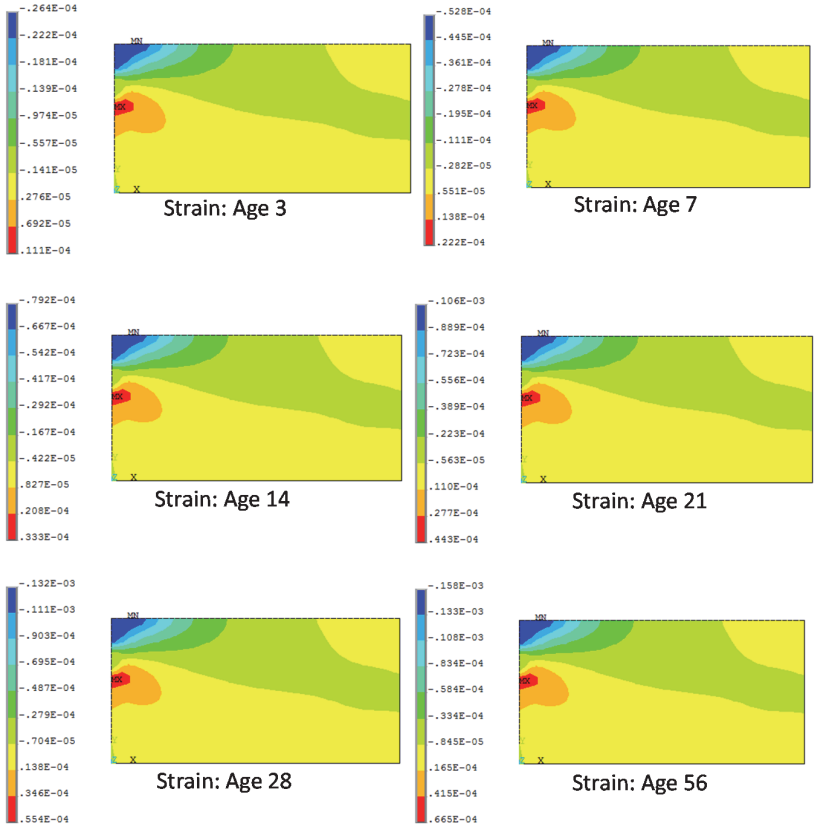

Fig. 13. Horizontal strain: 2D plain strain FEA simulated under no-slip condition

4. Numerical Analysis & Simulations

The initial de-bonding FEA simulations implemented here was based on the corresponding values of the curvature estimated for each overlay thickness considered. The simulations investigate ensuing progressive de-bonding due to intrinsic net peeling strain. The effects of parameters like varying relative stiffness and compressibility of the bonded bi-material, overlay structural scale, creep coefficient and numerical oscillatory phase-angle at de-bonding tip were studied unequivocally. In the FEA model, the intrinsic edge warping/curling was idealised as a uniaxial edge-stress condition such that the induced cohesive interfacial stresses were assumed developing hypothetically along a 2D de-bonded edges rather than on the entire slab interface. In this respect, a 2-D plane strain analysis would suffice (Houben, 2003; Mei et al., 2007).

Table 7. Elastic Mismatched Properties between RC-SFR-PMC and OPCC

Model No	RC-SFR-PMC Elastic Modulus E_1 (GPa)	OPCC Elastic Modulus E_2 (GPa)	Estimated Relative Stiffness (α)	Estimated Relative Compressibility (β)
1	16.68	22.3	-0.10	0.04
2	18.44	22.3	-0.06	
3	20.61	22.3	-0.02	
4	22.75	22.3	0.03	
5	25.76	22.3	0.08	
6	27.68	22.3	0.11	

Edge warping/curling was induced using the corresponding edge curvature estimated for variable overlay thickness of 50, 75, 100 and 125mm. The substrate thickness and working length were maintained at 150mm and 1000mm respectively – similar to the test specimen shown in Fig. 10. The FEA model meshing for the substrate and overlay was accomplished with a 2-D Structural Solid element (PLANE182). The element is defined by four nodes having two degrees of freedom per node. The interface between the bonded materials was discretized by a set of target segment using TARGE169 paired with its associated contact surface element (CONTA171). The characterisation of the interface and the bi-material was based on the values shown in Table 7 and Table 8. For de-bonding to propagate, it's assumed that the critical cracking is reached along the zero-thickness interface.

Table 8. Interfacial Fracture parameters for Mode I and Mode II

Failure Mode	Interface Cohesive Failure Criteria			Interface Evolution Contact Parameters	
	Interfacial Bond Strength(MPa)	Fracture Resistance (N/m)	Critical Opening/slip limit (mm)	Cohesion (MPa) (C)	Friction coefficient (μ)
Mode I	2.10	35.4	0.03	1.63	0.8
Mode II	3.31	143	0.11		

4.1 Result Analysis and Discussion

In the FEA model, two cases were considered based on the loading magnitude. The first loading case adhered to the estimated overlay edge curvature derived from equation 14 for each overlay thickness. The interface only attains its critical de-bonding condition when the mixed-mode energy release rate G_{ic} equals the fracture toughness of the interface $G_{ic}(\Psi)$. Based on Table 8, the condition for mixed mode critical de-bonding is reached when $G_{ic}(\Psi) = 109.8\,J/m^2$ or mixed critical cracking $u_m^c = 0.056mm$. In Fig. 14(a), which depicts the computed FEA interface energy release rate for each test specimen, it is clear that the peeling strain loading effect of the imposed curvature on the interface is generally small and will not be sufficient to cause any critical de-bonding of the overlay. The maximum value shown here is $20.03\,J/m^2$ which is only about 18.2% of the interface fracture toughness. Also, it is observed that the interface energy release rate varies as a function of the bi-material relative stiffness and overlay structural scale. However, the two variables seem to lose effects as the overlay structural scale (η) approaches 0.50 ($h_{overlay} \rightarrow h_{substrate}$). The general indicative trend shows that the rate of energy release in compliant overlay bonded on relatively stiffer substrate (when $\alpha < 0$) is higher than in a more compliant substrate (when $\alpha > 0$). Thus, a more compliant overlay generally provides less relative constraint against bending induced de-bonding. The second loading case was based on doubling the magnitude of the estimated curvature (assuming excessive shrinkage strain is envisaged). As seen in Fig. 14(b), similar trend of response is observed when the applied curvature is doubled for each test specimen. However, under the current loading, critical de-bonding condition is observed for compliant overlay ($\alpha \leq -0.06$) when overlay thickness $h_{overlay} \leq 64.3mm$ (i.e. η → 0.3). As such, it is predicted that overlay thickness in the proximity of 75mm and 100mm will be sufficient to resist critical de-bonding where possible excessive overlay shrinkage is envisaged at the early age of casting. This kind of study is pertinent for quick check analysis, when designing a bonded concrete overlay design scheme for pavements, bridges, etc.

In addition, in Fig. 14 (c, d) the variation of the ensuing numerical phase-angle (Ψ) around the oscillatory field (see Fig. 1b) is shown. As seen the phase angle is primarily influenced by the structural scale (η) - the effect of material relative stiffness (α) seems to be inconsequential for bending related de-bonding. The phase-angle, and by extension its effect on the interface energy release rate decreases with increased structural scale. In dimensionless term, Fig. 15 is illustrated to depict the restraint capacity of the overlay sequel to equation 10. Here, the value of the de-bonding restraining coefficient

(D_c) can also be used to predict the associated cohesive zone length (L_{cz}) during de-bonding via $L_{cz} = D_c(E^*.G_{ic}(\Psi)/\lambda_m^2)$. In Fig. 15(a , b), it is evident that the restraint capacity of the interface increases with increased overlay elastic stiffness and thickness, while the accompany cohesive zone length decreases with increased overlay structural scale and elastic stiffness. In addition, the observed effects of creep coefficient (ϕ) on D_c and L_{cz} is seen in Fig. 15(c & d). The values of elastic relative stiffness (α) shown in Fig. 15(c & d) are contingent on the modified values of elastic moduli given in Table 8 based on: $E_1^* = \left(\frac{E_1}{1+[\phi(t,t_0)]}\right)$. While it is true that stresses in the overlay are relieved due to creep coefficient $[\phi(t,\ t_0)]$ effects on the overlay elastic modulus, its composite resultant effects show that the overlay becomes more and more compliant relative to the substrate material, which makes it somewhat less resistant to de-bonding failure.

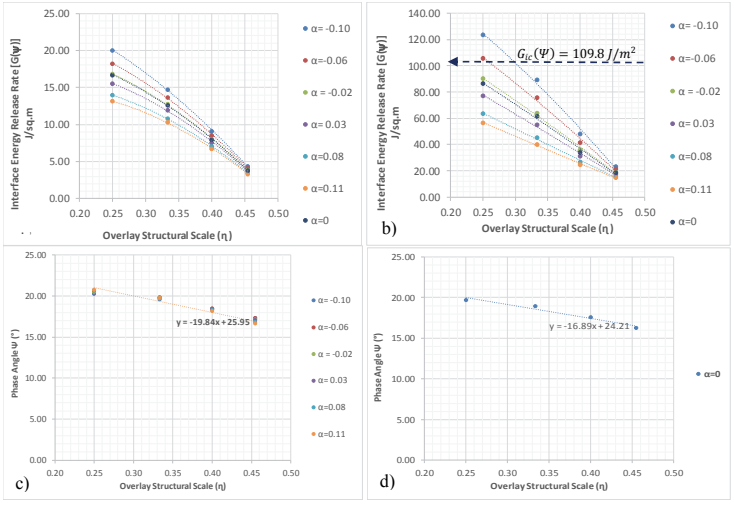

Fig. 14. (a & b) Interface Energy Release Rates for variable edge curvature loading (c & d) Phase angle variation as a function of bi-material relative stiffness and Overlay Structural Scale.

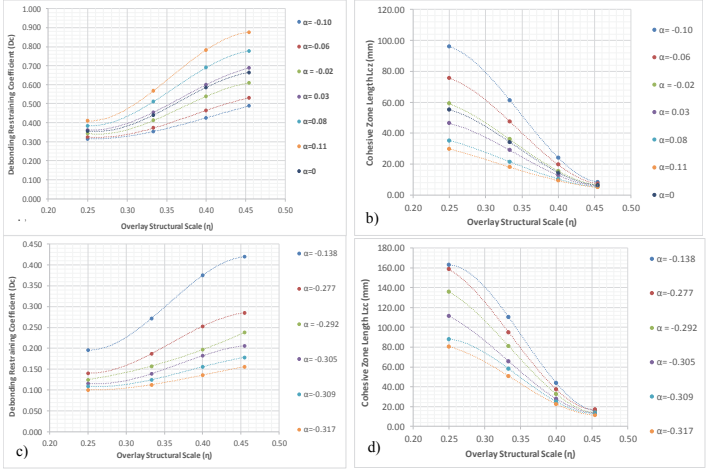

Fig. 15. (a & b) De-bonding Restraining Coefficient & Cohesive zone length variations as a function of the bi-material relative stiffness and Overlay Structural Scale, (c & d) Effects of Creep coefficient on De-bonding Restraining Coefficient & Cohesive zone length

5. Conclusions

From the above analysis and discussions, it is clear that the use of numerical methods provides a quick, robust and economical way of modelling and testing cementitious composite materials and structural systems when properly calibrated with reliable experimental data. In the analysis, both statistical optimisation and finite element techniques were employed with the following findings:

1. The high cement content typically required for bridge and pavement overlay materials modified with SBR can safely be reduced with appropriate blend of pozzolanic material like high reactive Metakaolin without compromising strength and interfacial bonding.
2. The RC-SFR-PMC overlay material in the above investigations achieves its optimum plastic performance with about 30% cement replacement with Metakaolin. This is desirable, and in tandem with the global overall sustainability goal for the construction industry.
3. The optimum mixture achieves full consolidation at about 36sec. consistency with a corresponding AMD falling above 98% of the mix's TAFD. These values are well within the recommended limits in the codes of practice.
4. The interfacial bond and fracture properties show that the optimum mix exhibits excellent composite compatibility and stability with the OPCC substrate, with no noticeable de-bonding or excessive shrinkage observed. The mean bond strengths achieve 2.10 MPa and 2.50 MPa tensile and 3.31 MPa and 4.17 MPa shear at 3 and 28 days respectively. Similarly, interfacial fracture toughness yielded about 35N/m and 65N/m in mode I and 143 N/m and 271 N/m in mode II at 3 and 28 days respectively.
5. The applied curvature on the FEA model due to the measured shrinkage strain is inadequate to cause critical de-bonding. The maximum resulting interface energy release rate only attains about 18% of the effective interface fracture toughness.
6. For plane strain conditions, the rate of interface energy release varies as a function of the bi-material relative stiffness and overlay structural scale. However, the two variables lose effects as the overlay structural scale approaches 0.50. The general indicative trend shows that the rate of energy release in compliant overlay when $\alpha < 0$ is higher than when $\alpha > 0$. Therefore, a more compliant overlay generally provides less relative constraint to bending induced de-bonding.
7. By doubling the applied curvature, critical de-bonding condition is reached for compliant overlay ($\alpha \leq -0.06$) when structural scale ($\eta = 0.3$). Thus, it is envisaged that overlay thickness in the proximity of 75mm and 100mm will be sufficient to resist critical de-bonding where possible excessive overlay shrinkage is predicted at the early age of casting/curing.
8. The observed numerical local phase angle around the oscillatory field at crack tip is primarily influenced by the structural scale (η). The effects of the material relative stiffness (α) is trivial in bending related de-bonding.
9. The restraint capacity of the interface increases with increased overlay elastic stiffness and thickness, while the accompany cohesive zone length decreases with increased overlay structural scale and elastic stiffness.
10. Stresses in the overlay are relieved due to creep coefficient $[\phi(t,\ t_0)]$ effects, but its overall composite resultant effects show that the overlay becomes more and more compliant with less resistant to critical de-bonding.

Compliance with Ethical Standards: This study was partly funded by Aggregate Industries UK. The authors also acknowledge the support of Tarmac Ltd UK for providing some of the materials used for this research.

Conflict of Interest: The authors declare that they have no conflict of interest.

References

ACI 548.1R-92 (1992). Guide for the use of polymers in concrete. ACI Committee Report, Farmington Hills.

ACI 548.4-93 (1993). Standard specification for latex modified concrete overlays. ACI Committee Report, Farmington Hills.

ACI 211.3R (2002). Guide for selecting proportions for no-slump concrete. ACI Committee Report, Farmington Hills, Ml, USA.

Alfano, G., & Crisfield, M.A. (2001). Finite Element Interface Models for the Delamination Anaylsis of Laminated Composites: Mechanical and Computational Issues, *International Journal for Numerical Methods in Engineering*, 501701-1736.

Aliha, M. R. M., Heidari-Rarani, M., Shokrieh, M. M., & Ayatollahi, M. R. (2012). Experimental determination of tensile strength and K (IC) of polymer concretes using semi-circular bend(SCB) specimens. *Structural Engineering and Mechanics*, *43*(6), 823-833.

ASTM C469/C469M (1994). Standard Test Method for Static Modulus of Elasticity and Poisson's Ratio of Concrete in Compression. ASTM International, USA.

ASTM C1439-99 (1999). Standard test methods for polymer-modified mortar and concrete. ASTM International, USA.

ASTM C138 (2001). Standard test method for density (unit weight), yield, and air content (Gravimetric). ASTM International, USA.

ASTM C1170 / C1170M – 08 (2008). Standard Test Method for Determining Consistency and Density of Roller-Compacted Concrete Using a Vibrating Table. ASTM International, USA.

ASTM D792 (2008). Standard Test Methods for Density and Specific Gravity (Relative Density) of Plastics by Displacement. ASTM International, USA.

ASTM C496/C496M-11 (2011). Standard test method for splitting tensile strength of cylindrical concrete specimens, ASTM International, USA.

Birkeland, H. W. (1960, May). Differential shrinkage in composite beams. *Journal Proceedings, 56*(5), 1123-1136).

Bower, A.F. (2010). *Applied Mechanics of Solid*, Taylor and Francis Group, LLC.

Box, G.E.P., & Draper, N.R. (1987). *Empirical Model-Building and Response Surfaces*, 1st edn. John Wiley & Sons Inc.

Buyukozturk, O., & Hearing, B. (1998). Crack propagation in concrete composites influenced by interface fracture parameters, *International Journal of Solids and Structures*, *35*(31-32) 4055 – 4066.

BS 598-3 (1985) Sampling and examination of bituminous mixtures for roads and other paved areas, Methods for design and physical testing. British Standard Institute.

BS EN 12390-6 (2000). Testing hardened Concrete. Testing Splitting Strength of test specimens. *British Standard Institute.*

Caballero, A., Willam, K.J., & Carol, I. (2008). Consistent tangent formulation for 3D interface modeling of cracking/fracture in quasi-brittle materials, *Computer Methods in Applied Mechanics and Engineering, 197*(33-40)*,* 2804 - 2822.

Carlsson, L.A. and Prasad, S., (1993). Interfacial fracture of sandwich beams, *Engineering Fracture Mechanics*, *44*(4) 581 – 590.

Chandra, N. (2002). Evaluation of interfacial fracture toughness using cohesive zone model, *Composite: Applied science and manufacturing*, Part A, *33*, 1433 – 1447.

Charalambides, P. G., Cao, H.C. Lund, J., & Evans, A.G. (1990). Development of a test method for measuring the mixed mode fracture resistance of bimaterial interfaces, *Mechanics of Materials*, *8*, 269 – 283.

Cornec, A., Scheider, I., & Schwalbe, K. (2003). On the practical application of the cohesive model, *Engineering Fracture Mechanics*, *70*(14), 1963-1987.

Dundurs, J. (1969). Edge-Bonded Dissimilar Orthogonal Elastic Wedges Under Normal and Shear Loading, *ASME Journal of Applied Mechanics*, *36*, 650 – 652.

Enfedaque, A., Alberti, M. G., Paredes, J. A., & Gálvez, J. C. (2017). Interface properties of polyolefin fibres embedded in self-compacting concrete with a bond improver admixture. *Theoretical and Applied Fracture Mechanics*, *90*, 287-293.

Eurocode 2 (BS EN, 1992). Design of concrete structures.

Fakhri, M., Amoosoltani, E., & Aliha, M. R. M. (2017). Crack behavior analysis of roller compacted concrete mixtures containing reclaimed asphalt pavement and crumb rubber. *Engineering Fracture Mechanics*, *180*, 43-59.

Guan, J. F., Hu, X. Z., Xie, C. P., Li, Q. B., & Wu, Z. M. (2018). Wedge-splitting tests for tensile strength and fracture toughness of concrete. *Theoretical and Applied Fracture Mechanics*, *93*, 263-275.

Hillerborg, A., Modeer, M. and Petersson, P.E. (1976). Analysis of crack formation and crack growth in concrete by means of fracture mechanics and finite elements, *Cement and Concrete Research*, *6*, 773 – 782.

Karadelis, J. N., & Lin, Y. (2017). Strain energy release rate at interface of concrete overlaid pavements. *International Journal of Pavement Engineering*, *18*(12), 1060-1069.

Kim, M. O., Bordelon, A. C., & Lee, N. K. (2017). Early-age crack widths of thin fiber reinforced concrete overlays subjected to temperature gradients. *Construction and Building Materials*, *148*, 492-503.

Kim, M. O., & Bordelon, A. C. (2017). Cracking and debonding of thin fiber reinforced overlays (No. MPC 17-319).

Heidari-Rarani, M., Aliha, M. R. M., Shokrieh, M. M., & Ayatollahi, M. R. (2014). Mechanical durability of an optimized polymer concrete under various thermal cyclic loadings–An experimental study. *Construction and Building Materials*, *64*, 308-315.

Houben, L. J. M. (2003). Structural design of Pavement – Part IV: Design of Concrete Pavements, Lecture Notes CT4860, Faculty of Civil Engineering and Geosciences, TU Delft; Delft.

IDOT (2000). Test Method number Iowa 406-C: method of test for determining the shearing strength of bonded concrete. Iowa Department of Transportation, Ames.

Mei, H., Pang, Y., & Huang, R. (2007). Influence of Interfacial delamination on Channel cracking of elastic thin-films, *International Journal of Fracture, 148*, 331 – 342.

Mirsayar, M., Shi, X., & Zollinger, D. (2017). Evaluation of interfacial bond strength between Portland cement concrete and asphalt concrete layers using bi-material SCB test specimen. *Engineering Solid Mechanics*, *5*(4), 293-306.

Mu, F., & Vandenbossche, J. (2017). A superimposed cohesive zone model for investigating the fracture properties of concrete–asphalt interface debonding. *Fatigue & Fracture of Engineering Materials & Structures*, *40*(4), 496-511.

Myasnikov, V.P., Guzeev, M.A. & Ushakov, A.A. (2004). Self-equilibrated stress fields in a continuous medium. *Journal of Applied Mechanics and Technical Physics, 45*, 558.

Morgan, D.R. (1996). Compatibility of concrete repair materials and systems. *Construction and Building Material*, *10*(1), 57-67.

Nawy, E.G., & Ukadike, M.M. (1983). Shear Transfer in Concrete and Polymer Modified Concrete Members Subjected to Shearing Loads. *Journal of Testing and Evaluation, JTEVA, 11*(2), 89 – 98.

Olubanwo, A.O., & Karadelis, N.K. (2015). Interfacial Delamination Failure in Bonded Concrete Overlay Systems - A Review of Theories and Modelling Methods. *International Journal of Civil Engineering & Technology (IJCIET)*, *6*(5), 85-99.

Olubanwo A. O., & Karadelis J. N. (2015). Applied mixture optimization techniques for paste design of bonded roller compacted fibre reinforced polymer modified concrete (BRCFRPMC) overlays. *Journal of Materials and Structures*, 48(7) 2023-2042.

Olubanwo, A.O., Karadelis, J.N., Xu, Y., Lin, Y., & Phillips, P. (2016). Optimum design for sustainable, 'Green' concrete overlays. Part III: Interfacial delamination. Proceedings, *4th International Chinese European Workshop on Functional Pavement Design,* Delft University, The Netherlands, June/July 2016, 1465-1475.

Olubanwo, A.O., Karadelis, J.N., & Abbey, S.J. (2017). Evaluation of Equivalent Delamination Driving Coefficient in Bonded Concrete Overlays. *International Journal of Civil Engineering & Technology (IJCIET)*, *8*(5), 1436-1444.

Petersson, P.E. (1981). Crack Growth and Development of Fracture Zones in Plain Concrete and Similar Materials, *Report* TVBM – 1006, Division of Building Materials, Lund Inst. of Technology, Lund, Sweden.

Rooholamini, H., Hassani, A., & Aliha, M. R. M. (2018). Evaluating the effect of macro-synthetic fibre on the mechanical properties of roller-compacted concrete pavement using response surface methodology. *Construction and Building Materials*, *159*, 517-529.

Silfwerbrand, J. (1997). Stresses and Strains in Composite Concrete Beams subjected to Differential Shrinkage *ACI Structural Journal* 94(4).

Suprenant, B. (1988). Bonding new concrete to old, *Concrete Construction*, *33*(7), 676- 680.

Turon, A., Davila C.G., Camanho P.P., & Costa, J. (2007). An engineering solution for mesh size effects in the simulation of delamination using cohesive zone models. *Engineering Fracture Mechanics*, *74*, 1665–1682.